Forward electron emission produced in grazing ion-surface collisions: Dependence on the surface topography

G. R. Gómez, E. A. Sánchez,* and O. Grizzi*
Comisión Nacional de Energía Atómica, Centro Atómico Bariloche and Instituto Balseiro, 8400-San Carlos de Bariloche, Argentina
(Received 2 September 1997; revised manuscript received 2 January 1998)

We present measurements of electron emission produced in 64-keV H^+ grazing bombardment of Si(111) surfaces prepared with different topographies. The surfaces were initially irradiated with several fluences of Ar^+ at normal incidence, and their topographies characterized by an atomic-force microscope (AFM). The electron energy spectra, measured close to the direction of the projectile specular reflection, show two characteristic structures: a peak at an energy $E_{CE}=35$ eV, corresponding to electrons moving with the projectile velocity (convoy electrons), and a broad peak at an energy $E_M>E_{CE}$. Their relative intensities depend strongly on the surface roughness. A similar behavior was observed for GaAs(110) and Al(111) surfaces prepared with different *in situ* polishing methods. A code developed to process the AFM images allowed us to assign the electron structures at E_M and E_{CE} to specific topographic features. [S0163-1829(98)03116-6]

I. INTRODUCTION

Ion-surface collisions at grazing incidence are becoming an important tool to test surface properties with very high sensitivity to the last atomic layer. In particular, the ion-induced electron emission has been used to study surface magnetic properties[1,2] and overlayer growth.[3,4] Because of the high surface sensitivity, the emitted electron can be strongly affected by the topography of the target. In rough surfaces, close encounter collisions between impinging projectiles and target atoms at defects preclude planar channeling and produce a deeper penetration of some of the ions into the bulk of the solid. The electrons that recede from the surface at low emission angles may also sustain violent collisions with defects. In addition, there are important differences in the interaction of these outgoing electrons with the induced surface potentials due to the sudden variations in the distance to the surface. In this work we study the relation between the shape of the forwardly emitted electron energy distribution produced in grazing ion-surface collisions and the topographic structure of different surfaces.

Previous results show that for rough surfaces the emitted electron energy distributions, observed close to the direction of the reflected projectiles, are dominated by a peak centered at an energy $E_{CE}=m_eE_p/M_p$, with m_e and M_p the electron and ion masses, and E_p the projectile energy.[5–7] Because of its energy and angular distribution, this peak was assigned to electron capture and/or loss into continuum states of the projectile, and is usually referred to as a convoy peak. Instead, for smooth surfaces the electron energy distributions are dominated by a broad peak at an energy E_M somewhat higher than E_{CE}.[8–17] This peak at E_M was related to the surface ion-induced potential.[8,9,13,14,18] There are cases where both peaks (at E_M and E_{CE}) were observed in the same spectrum.[12,14–17] Sánchez *et al.*[14,15] showed a qualitative correlation between their relative intensities and the topography of a Si(111) surface annealed at different temperatures: with increasing surface roughness the intensity at E_M strongly decreased in comparison with that at E_{CE}. Because of the poor vertical resolution of the scanning microscope, the authors could not relate the peaks observed in the electron spectra with specific features of the surface topography. The aim of the present paper is to perform a systematic study of the variations of the emitted electron energy distribution with the surface topography, and to obtain information about the shape and size of the topographic features producing either the true convoy peak (at E_{CE}) or the shifted structure (at E_M). We present measurements of electron emission performed during H^+ grazing bombardment of Si(111) surfaces, which were previously prepared by irradiation with different fluences of Ar^+ at normal incidence. The topography was characterized by an atomic-force microscope (AFM). In order to make a quantitative analysis of the results we developed a code for processing the topographic images acquired with the AFM.

II. EXPERIMENT

The measurements were performed in an ultrahigh-vacuum (UHV) chamber,[19] equipped with standard facilities for Auger-electron spectroscopy (AES), sample sputtering, and annealing. The Ar^+ and H^+ ion beams were produced in a radio-frequency source, accelerated to 10–22 keV (Ar^+) and 64 keV (H^+), and mass analyzed by a magnet. Electrons ejected in a cone of half-angle $\theta_0=2°$ were energy analyzed with a resolution of 1% by a custom-made[19] rotatable cylindrical mirror analyzer. All the spectra were corrected for the transmission function of the analyzer and normalized to the incoming beam current, measured with a Faraday cage placed at the end of the beam line.

Two mirror polished Si(111) samples were prepared by irradiation with several fluences of 10 and 22 keV Ar^+ at normal incidence. The irradiation was performed in a secondary vacuum chamber with a base pressure of 10^{-7} Torr. The surface bombarded region was limited to a band of 1×6 mm by using slits placed at 40 mm from the sample. By moving the sample, it was possible to irradiate several well-defined regions of the surface, leaving a virgin region in between. One of the Si(111) samples, which we will refer as

TABLE I. Ion fluences used to modify the topography of an initially flat Si(111) surface.

10 keV $Ar^+ \rightarrow$Si(111) sample 1		22 keV $Ar^+ \rightarrow$Si(111) sample 2	
Region	Fluences (ions/cm^2)	Region	Fluences (ions/cm^2)
A	2.1×10^{16}	*A*	3.9×10^{16}
B	2.6×10^{16}	*B*	5.6×10^{16}
C	3.1×10^{16}	*C*	7.2×10^{16}

sample 1, was bombarded in three band regions (*A*, *B*, and *C*) with 10 keV Ar^+; the ion fluences are shown in Table I. The Si(111) sample 2 was irradiated with 22 keV of Ar^+ also in three regions (*A*, *B*, and *C*). We used an air operated AFM to characterize the topography of the samples. The apparatus was an Autoprobe CP from Park Scientific Instruments, calibrated in the *x*, *y*, and *z* directions with gratings consisting of steps of 1 μm pitch and 410 Å height, and inverted pyramids of 2500 Å pitch and 700 Å depth. We acquired several images for each bombarded region as well as for the nonirradiated regions. This procedure was done before and after placing the samples in the UHV chamber for the electron emission measurements. With the preparation method described above we obtained a variety of topographies consisting of structures of different sizes, with an average height ranging from 30 Å to 1500 Å.

Once placed in the UHV chamber, the Si(111) samples were cleaned by gentle cycles of 500 eV Ar^+ sputtering at 45° incidence and annealing at 450 °C, until no contamination was detected with AES. The electron energy distributions were measured with a proton beam collimated to irradiate a band region of 0.5 mm wide, i.e., smaller than the previously prepared bands.

III. RESULTS

Two different kinds of topographies were produced by Ar^+ irradiation at normal incidence and the subsequent cleaning cycles. Those regions of sample 1 bombarded with 10 keV Ar^+ present pits of several hundred angstroms depth and diameter, whose density increases in the regions irradiated with the higher Ar^+ fluences. Instead, the regions of sample 2 bombarded with 22 keV Ar^+ show blisterlike structures, whose density, height, and diameter depend on the Ar ion fluence. From the AFM images acquired before and after performing the sputtering and annealing cycles we conclude that these topographies were produced by the combination of blistering[20] and surface sputtering. During the irradiation at normal incidence, Ar clusters can be formed beneath the surface, these clusters have been observed in experiments of Ar ion implantation at 40 keV on Si(111) (Ref. 21) for irradiation doses ranging from 10^{16} up to 10^{17} ions/cm^2. The AFM images obtained before placing the samples in the UHV chamber show that the blisterlike structures were initially present in the irradiated-regions of both Si surfaces. After performing the cleaning cycles, pits appeared in sample 1, probably related to blisters the coverings of which had been removed by sputtering (the thickness of the blister cover depends on the implantation energy, corresponding thinner covers to lower energies). In the more irradiated regions of sample 2 there were some blisterlike structures with cracks

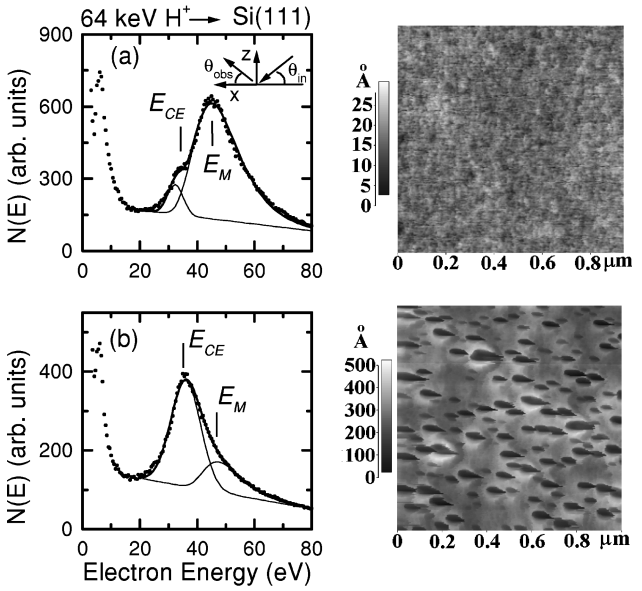

FIG. 1. (a) Left: energy spectra of electrons emitted from a non-previously-irradiated region of the Si(111) sample 1. Full lines: fitting curves for the peaks at E_{CE} and E_M. Inset: Schematic diagram of the scattering geometry, the observation is in the scattering plane $(x-z)$ at an elevation angle $\theta_{obs}=\theta_{in}=1°$. Right: AFM image of the respective surface region. (b) Same as (a) for a region of the same sample previously irradiated with 10 keV Ar^+ ions (fluence: 3.1×10^{16} ions/cm^2).

on top after the cleaning cycles, these were formed when the blister covers were partially broken by either sputtering or the inner pressure exerted by the implanted gas.

We measured energy distributions of electrons emitted along the direction of the projectile specular reflection during 64 keV H^+ grazing bombardment of both Si samples. The incidence angle, measured with respect to the surface plane, was set to $\theta_{in}=1°$ [inset of Fig. 1(a)]. The ion-beam direc-

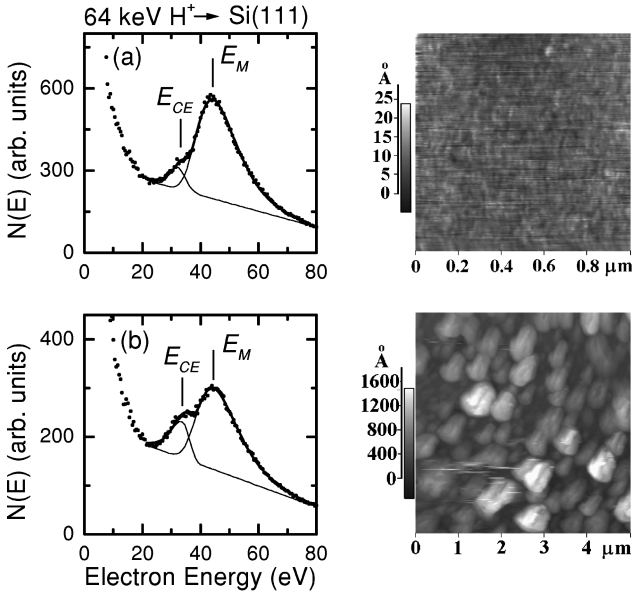

FIG. 2. (a) Same as Fig. 1(a) for Si(111) sample 2. (b) Same as Fig. 1(b) for a region of Si(111) sample 2 previously irradiated with 22 keV Ar^+ ions (fluence: 7.2×10^{16} ions/cm^2).

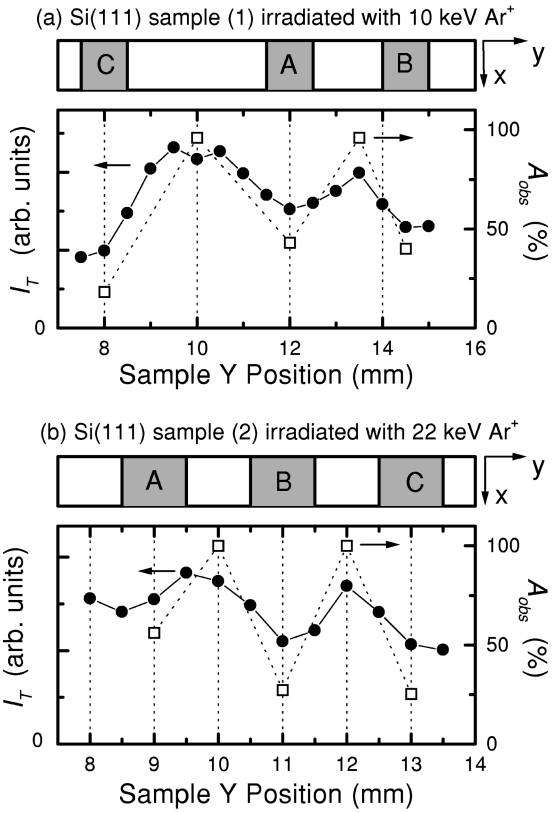

FIG. 3. (a) Total electron emission intensity I_T (●) and surface observable fraction $A_{\rm obs}$ (□) as a function of the y position of the Si(111) sample 1. Upper plot: top view of the surface, the gray zones represent previously Ar^+ irradiated regions (see Table I for the ion fluences). (b) Same as (a) for Si(111) sample 2.

tion was set parallel to the surface irradiated bands (x direction). For each Si surface we measured spectra by moving the sample in steps of 0.5 mm in the y direction, which is perpendicular to the scattering plane and to the irradiated bands. Figures 1 and 2 show two typical spectra for each sample. These distributions come from (a) a non-previously-irradiated region, and (b) from the region irradiated with the higher Ar^+ fluence (band C for both samples). Also displayed in the figures are the AFM images typical to each surface region. These topographic images were acquired after the electron emission measurements had been performed. The size of the scanned area is indicated at the bottom of each image, and at the left side we show the relation between the gray scale and the height in angstroms.

We can see in Figs. 1 and 2 that the electron energy distributions near E_{CE} are strongly dependent on the sample topography. For the smoother surfaces [spectrum (a) in both figures] a prominent structure is observed at $E_M \sim 45$ eV, with a shoulder at $E_{CE}=35$ eV (the latter corresponding to the convoy electron energy for H^+ at 64 keV). Instead, for the rougher surfaces [spectra (b)], the intensity of the peak at E_{CE} increases in comparison with that of the peak at E_M. We also observe in the figures that the peaks at E_M and E_{CE} are superimposed on the high-energy tail of the secondary electron background, whose intensity decreases for the rough surfaces, while its maximum remains approximately at the same position (6 eV). The variation of the relative intensity of the peak at E_{CE} with respect to that at E_M cannot be

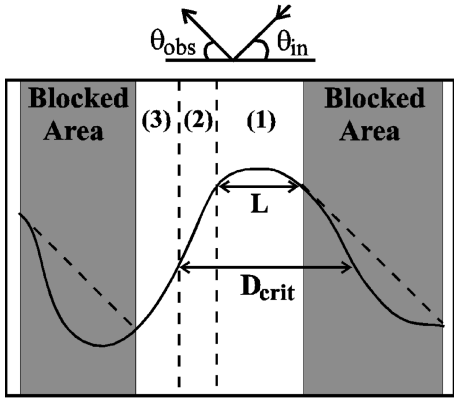

FIG. 4. Schematic diagram of the topographic line analysis. The directions of incidence and observation are shown in the upper plot. The observable region (white) is divided into (1) the smooth region of length L, (2) the convoy region, and (3) the remainder of the nonblocked region. $D_{\rm crit}$: critical ion penetration length for convoy electron production.

related to the root-mean-square deviation of the surface height distribution (rms height roughness). The rms height roughness obtained from the AFM images of the surface band regions corresponding to the spectra (b) were ~ 70 Å for sample 1 and ~ 300 Å for sample 2; however, the electron energy distribution showed a more pronounced peak at E_{CE} in the first case than in the second one. This result indicates that a more detailed analysis of the surface topography is required to interpret the behavior of the electron emission.

IV. DISCUSSION

An interesting feature seen in Figs. 1 and 2 is that the total forward electron emission decreases for the previously irradiated regions. In Fig. 3 we show the total electron intensity I_T measured at $\theta_{\rm obs}=1°$ and $\theta_{\rm in}=1°$ as a function of the y position of the sample. I_T was estimated from the electron energy distribution, by performing an integration of the spectrum from 0.5 to 100 eV. We can see in this figure that I_T decreases for the earlier irradiated regions, and that this reduction is more pronounced in the bands irradiated with the higher Ar^+ fluences. If the observation is at grazing angles, there are large areas where the electrons ejected from a rough surface are blocked in their outgoing path by defects (these regions are not observable from the detector). In order to make an evaluation of the size of these regions, we developed a computer program for processing the AFM images. For fixed directions of observation the program analyzes the AFM topographic image line by line, discriminating the surface regions that can not be seen by the detector. We define $A_{\rm obs}$ ($\theta_{\rm obs}$) as the fraction of the surface that is observable from a detector placed at $\theta_{\rm obs}$. In Fig. 3 we show with open squares the $A_{\rm obs}$ resulting from processing the AFM images of several band regions in both Si surfaces. The $A_{\rm obs}$ values were calculated as the average over the results obtained with various AFM images of different scan sizes and positions for each region. The size of the AFM scan was chosen several times larger than the typical topographic structures. We can see in this figure that there is a correlation between the be-

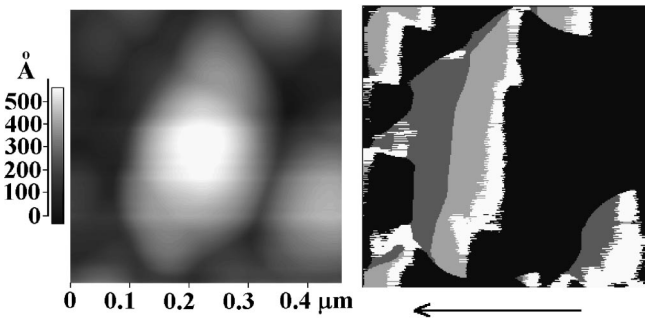

FIG. 5. Left: AFM image acquired for region C of Si(111) sample 2. Right: the same AFM image after processing. The smooth region is shown in white, the convoy region in light gray, the remainder of the observable region in dark gray, and the nonobservable region in black. Horizontal arrow: direction of observation.

havior of I_T and that of the observable areas ($A_{\rm obs}$). Although the general trends of the experiment are reproduced, a quantitative comparison would require a calculation accounting for the number of electrons ionized along the projectile path and their escape probability, which is beyond the scope of the present work.

The qualitative agreement obtained encourages us to study, with some modifications of the program, the dependence of the convoy electron emission on the surface topography. Most of the models proposed to describe the peak at E_M in high-energy ion-surface collisions were based on the repulsive effect of the ion-induced potential $\varphi_{\rm ind}$ (for a detailed description of $\varphi_{\rm ind}$ see Ref. 22). Hasegawa, Kimura, and Manhami[8] suggested that the convoy electrons are accelerated by $\varphi_{\rm ind}$, instead Reinhold *et al.*[18] proposed that the shifted structure is determined by rainbow scattering of the electrons in the screened field of the ion. In both models, the shape of the ion-induced potential and the geometry of the collision play an important role, requiring that the projectiles sustain grazing trajectories in atomically flat surface regions. In the first model it is also needed a long interaction time with $\varphi_{\rm ind}$. If the surface flatness is lost, these conditions are not fulfilled and, as it was experimentally observed, the outgoing electron energy distribution presents a broad peak at E_{CE}. Both models have been used to describe experiments at projectile energies higher than 300 keV/amu.[13,18] In our energy range there are no calculations of the convoy emission effect. A study of the size and shape of the surface regions producing the peak at E_M may help to clarify the origin of this peak.

In order to make a quantitative analysis we estimated the intensity of the peaks at E_M and E_{CE} (I_{EM} and I_{ECE}, respectively). Since no detailed information about the background is available, we tried to fit it at both sides of the peaks with different functions. Because the peaks at E_M and E_{CE} are well separated from the secondary electron maximum and superimposed on a smooth varying background region, a linear interpolation resulted reasonable. After performing the background subtraction, we adjusted the two peaks in the experimental energy distributions with fitting functions. The I_{EM} and I_{ECE} values were obtained from the total area of the respective functions. An example of this procedure is presented in Figs. 1 and 2, where we show the best fitting curves obtained for these spectra. We used Gaussian functions for the peaks at E_{CE} and three-parameter asymmetric peak functions for the structures at E_M $\{f(E)=A\ \exp(-\exp(-\xi)-\xi+1)$, where $\xi=(E-E_M)/w\}$. Although there are some differences in the position of the peak maxima, the values of I_{EM} and I_{ECE} evaluated from these fittings differ within 5% from those obtained with other sets of fitting curves (two Gaussian functions or combinations of Gaussian and asymmetric peak functions). It can be observed from the spectra that the width at half-height of the peak at E_{CE} was $\sim$10–15 eV. This broadening could be partially ascribed to the screening of the Coulombic ion potential[6] and, as it will be discussed later, to the energy loss of the projectiles that penetrate into the solid before being scattered off the surface.

We modified the image processing code to discriminate from the observable surface regions those sufficiently smooth, where the electrons receding at low observation angles can sustain grazing trajectories for several lattice constants. In Fig. 4 we show an schematic diagram of a surface side view along a direction within the scattering plane. We indicate in gray the regions that are not observable by the electron analyzer because they are blocked by defects. We further divide the observable region into three parts (vertical dashed lines): (1) the smooth region, where the slope of the tangent to the surface is lower than $\alpha=\tan(\theta_{\rm crit})$ (the angle $\theta_{\rm crit}$ is a parameter), (2) the convoy region, which does not meet the smoothness condition, but fulfills the condition that the ion path inside the material is lower than a parameter $D_{\rm crit}$, and (3) the remaining of the observable region. We assumed that the structure at E_M was formed by electrons emitted from regions of type (1). We imposed, in this case, an additional constraint on the size of these regions. Their length L along the direction of the ion path must be large enough ($L>L_{\rm crit}$) to allow grazing trajectories (with $L_{\rm crit}$ an adjustable parameter). We assumed that the electrons emitted from type (2) regions with velocities near v_p presented an outgoing distribution centered at E_{CE} (Convoy electrons). The ions receding from these regions must usually have traveled several lattice constants inside the solid before leaving the surface (as in foil transmission experiments). For large penetration distances the energy and angular straggling are so high, that almost all of the electrons produced with velocities near v_p contribute to the low-energy tail of the measured convoy distribution or are not detected. In our model, $D_{\rm crit}$ was a measure of the maximum distance that the ions can travel inside the solid, without being scattered at angles larger than the acceptance of the analyzer (2°) and with energy losses lower than the maximum expected from the experimental width of the convoy peak. We estimated $D_{\rm crit}$ $\sim$1500 Å, based on TRIM (Ref. 24) calculations of the energy and angular distributions for 64 keV H^+ transmitted through thin Si foils of different thickness. Finally, the electrons that recede from type (3) regions can contribute to the background distribution.

We define A_{EM} (A_{ECE}) as the smooth (rough) fraction of the surface area that, within our model, generates electron distributions centered at E_M (E_{CE}), i.e., region (1) (region (2)] in Fig. 4. There are three parameters ($\theta_{\rm crit}$, $L_{\rm crit}$, and $D_{\rm crit}$) to be adjusted. From these, $D_{\rm crit}$ was fixed by the criteria described above. Assuming that there are not large differences between the total cross sections for the mechanisms producing the peaks at E_{CE} and E_M, we compared the

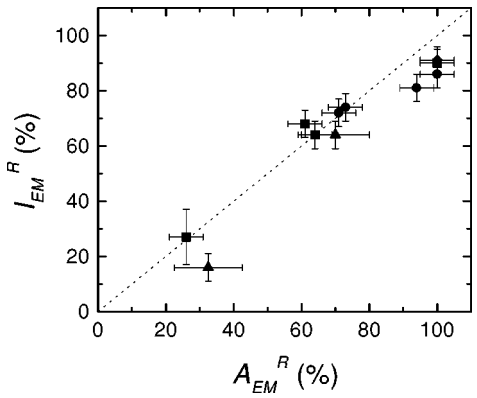

FIG. 6. Relative intensity of the peak at E_m (I_{EM}^R) as a function of the relative smooth area (A_{EM}^R) for Si(111) sample 1 (■), Si(111) sample 2 (●), Al(111) (▲), and GaAs(110) (♦), with different topographies.

relative intensity of the peak at E_M ($I_{EM}^R = I_{EM}/(I_{EM} + I_{ECE})$) with the relative smooth surface fraction [$A_{EM}^R = A_{EM}/(A_{EM}+A_{ECE})$]. We obtained a good agreement between both quantities for $\theta_{\rm crit} = 5° \pm 1°$ and $L_{\rm crit} = (100 \pm 30)$ Å.

In Fig. 5 we present an AFM image (left) of band region C in sample 2, and the corresponding processed image (right). The observation is in the direction shown by the arrow, with the elevation angle covering the range 0–3° (determined by $\theta_{\rm obs} \pm \theta_0$). We used different shades of gray to discriminate the smooth region (white), the convoy region (light gray), the remaining of the observable region (dark gray), and the nonobservable region (black).

In Fig. 6 we present the relative intensity I_{EM}^R as a function of the A_{EM}^R obtained from the processing of the AFM images. The I_{EM}^R error was estimated from a comparison of the results obtained by adjusting the peaks and background with several fitting functions. The error in A_{EM}^R was estimated from the scattering of the results obtained after processing various AFM images with different scan sizes and positions for the same surface band region. We can see in the figure that there is a linear relationship between I_{EM}^R and A_{EM}^R, with a proportionality constant γ approaching 1. We also present in this figure the data obtained with a smooth GaAs(110) surface and an Al(111) sample. In these cases the electron energy distributions were measured for 70 keV H^+ grazing bombardment, keeping the other experimental parameters the same as those described for the Si samples. The two points obtained for the Al surface correspond to the results obtained from the electron spectra and the AFM images acquired before and after performing several cycles of grazing Ar^+ sputtering and subsequent annealing, in order to reduce the roughness produced by the mechanical polishing.[23] We observe in the figure that the data follow the general trends observed for the Si(111) samples. In these cases, the processing of the AFM images was done with the same parameters used for the Si samples ($\theta_{\rm crit} = 5°$, $L_{\rm crit} = 100$ Å, and $D_{\rm crit} = 1500$ Å).

V. CONCLUSIONS

We measured energy distributions of electrons emitted forwardly during H^+ grazing collisions with Si, GaAs, and Al samples. The surfaces present a wide variety of topographies obtained by irradiation with several fluences of Ar^+ (in the case of Si) or by different cleaning methods (Al). The spectra show strong variations of the electron structures at E_M and E_{CE}: for increasing surface roughness the intensity of the peak at E_M decreases in comparison with that at E_{CE}. Based on a code developed to analyze the surface topography from AFM images, we have related the intensity of the peaks at E_{CE} and E_M with specific topographic features of the samples. In particular, the appearance of the shifted structure at $E_M \sim 45$ eV is ascribed to the presence of microscopically smooth surface regions with mean slope variations lower than 5°, and of at least 100 Å long. In these regions the grazing emitted electrons can interact with the ion-induced potential during several lattice constants, and sustain outgoing trajectories not blocked by defects. The Convoy peak at $E_{CE} = 35$ eV is related to electrons emitted in correlation with a reflected projectile, but receding from rough surface regions, i.e., those that do not meet the conditions just described. As a consequence of the geometry of the outgoing trajectory, these electrons do not have a long interaction time with the induced potentials, and the postcollisional evolution is dominated by the Coulomb interaction with the ion.

The results presented in this paper show that the analysis of the forward electron emission produced in grazing ion-surface collisions can be a useful tool to obtain information on the surface topography, in particular, concerning the relative fractions of smooth and rough regions.

ACKNOWLEDGMENTS

We acknowledge M. L. Martiarena and V. H. Ponce for useful discussions, H. Winter for providing the Si samples, and C. Wenger, J. De Pellegrin, and E. Sauro for their technical assistance in the experimental setup. We also acknowledge financial support from CONICET (Grant No. PMT-PICT0437) and Cooperativa de Electricidad Bariloche.

*Also at Consejo Nacional de Investigaciones Científicas y Técnicas, Argentina.

[1] C. Rau, K. Waters, and N. Chen, Phys. Rev. Lett. **64**, 1441 (1990).

[2] Carl Rau, Prog. Surf. Sci. **46**, 135 (1994).

[3] R. Pfandzelter and J. Landskron, Phys. Rev. Lett. **70**, 1279 (1993).

[4] R. Pfandzelter, T. Igel, and H. Winter, Surf. Sci. **389**, 317 (1997).

[5] L. F. de Ferrariis and R. Baragiola, Phys. Rev. A **33**, 4449 (1986).

[6] H. Winter, P. Strohmeier, and J. Burgdörfer, Phys. Rev. A **39**, 3895 (1989).

[7] E. A. Sánchez, M. L. Martiarena, O. Grizzi, and V. H. Ponce, Phys. Rev. A **45**, R1299 (1992).

[8] M. Hasegawa, K. Kimura, and M. Mannami, J. Phys. Soc. Jpn. **57**, 1384 (1988).

[9] A. Koyama, Y. Sasa, H. Ishikawa, A. Misu, K. Ishii, T. Iitaka, Y. H. Ohtsuki, and M. Uda, Phys. Rev. Lett. **65**, 3156 (1990).

[10] H. Ishikawa, A. Misu, A. Koyama, T. Iitaka, M. Uda, and H.

Ohtsuki, Nucl. Instrum. Methods Phys. Res. B **67**, 160 (1992).
[11] Y. Mizuno, M. Hasegawa, Y. Susuki, K. Kimura, and M. Mannami, Nucl. Instrum. Methods Phys. Res. B **67**, 164 (1992).
[12] A. Koyama, Nucl. Instrum. Methods Phys. Res. B **67**, 103 (1992).
[13] K. Kimura, M. Tsuji, and M. Mannami, Phys. Rev. A **46**, 2618 (1992).
[14] E. A. Sánchez, O. Grizzi, M. L. Martiarena, and V. H. Ponce, Phys. Rev. Lett. **71**, 801 (1993).
[15] E. A. Sánchez, O. Grizzi, M. L. Martiarena, and V. H. Ponce, J. Phys.: Condens. Matter **5**, A289 (1993).
[16] E. A. Sánchez, O. Grizzi, G. Nadal, G. R. Gómez, M. L. Martiarena, and V. H. Ponce, Nucl. Instrum. Methods Phys. Res. B **90**, 261 (1994).
[17] G. R. Gómez, E. A. Sánchez, O. Grizzi, M. L. Martiarena, and V. H. Ponce, Nucl. Instrum. Methods Phys. Res. B **122**, 171 (1997).
[18] C. O. Reinhold, J. Burgdörfer, K. Kimura, and M. H. Mannami, Phys. Rev. Lett. **73**, 2508 (1994); C. O. Reinhold and J. Burgdörfer, Phys. Rev. A **55**, 450 (1997).
[19] L. F. de Ferrariis, F. Tutzauer, E. A. Sánchez, and R. A. Baragiola, Nucl. Instrum. Methods Phys. Res. A **281**, 43 (1989).
[20] O. Auciello, Radiat. Eff. **30**, 11 (1976).
[21] G. Faraci, S. La Rosa, A. R. Pennisi, S. Mobilio, and G. Tourrillon, Phys. Rev. B **43**, 9962 (1991).
[22] F. J. García de Abajo, and P. M. Echenique, Phys. Rev. B **46**, 2663 (1992).
[23] E. A. Sánchez, G. R. Gómez, J. E. Gayone, R. G. Pregliasco, and O. Grizzi, Acta Microsc. **5**, Suppl. B, 372 (1996).
[24] J. P. Biersack and L. G. Haggmark, Nucl. Instrum. Methods **174**, 257 (1980).